Received: 21 October 2016 | Accepted: 8 March 2017

DOI: 10.1111/jace.14895

ORIGINAL ARTICLE

Journal of the American Ceramic Society

X-ray tomography of feed-to-glass transition of simulated borosilicate waste glasses

William H. Harris[1] | **Donna P. Guillen**[2] | **Jaroslav Klouzek**[3] | **Richard Pokorny**[3] | **Tetsuji Yano**[4] | **SeungMin Lee**[5] | **Michael J. Schweiger**[5] | **Pavel Hrma**[5]

[1]Department of Chemical and Biomolecular Engineering, Department of Physics, North Carolina State University, Raleigh, North Carolina

[2]Materials Science and Engineering Department, Idaho National Laboratory, Idaho Falls, Idaho

[3]Laboratory of Inorganic Materials, Joint Workplace of the University of Chemistry and Technology Prague and the Institute of Rock Structure and Mechanics of the ASCR, Prague, Czech Republic

[4]Department of Chemistry and Materials Science, Tokyo Institute of Technology, Tokyo, Japan

[5]Pacific Northwest National Laboratory, Richland, Washington

Correspondence
William H. Harris, Department of Chemical and Biomolecular Engineering, Department of Physics, North Carolina State University, Raleigh, NC
Email: whharris@ncsu.edu

Funding information
Office of Nuclear Energy, Grant/Award Number: DE-AC07-05ID14517; DOE Office of Science

Abstract

High-level waste feed composition affects the overall melting rate by influencing the chemical, thermophysical, and morphological properties of a cold cap layer that floats on the molten glass where most feed-to-glass reactions occur. Data from X-ray computed tomography imaging of melting pellets comprised of a simulated high-aluminum feed reveal the morphology of bubbles, known as the primary foam, for various feed compositions at temperatures between 600°C and 1040°C. These feeds were formulated to make glasses with viscosities ranging from 0.5 to 9.5 Pa s at 1150°C, which was accomplished by changing the SiO_2/(B_2O_3+Na_2O+Li_2O) ratio in the final glass. Pellet dimensions and profile area, average and maximum bubble areas, bubble diameter, and void fraction were evaluated. The feed viscosity strongly affects the onset of the primary foaming and the foam collapse temperature. Despite the decreasing amount of gas-evolving components (Li_2CO_3, H_3BO_3, and Na_2CO_3), as the feed viscosity increases, the measured foam expansion rate does not decrease. This suggests that the primary foaming is not only affected by changes in the primary melt viscosity but also by the compositional reaction kinetic effects. The temperature-dependent foam morphological data will be used to inform cold cap model development for a high-level radioactive waste glass melter.

KEYWORDS

borosilicate glass, computed tomography, glass melting, morphology, nuclear waste, X-ray

1 | INTRODUCTION

Plutonium production operations, conducted by U.S. defense programs during the Cold War, have left the Hanford Site (in southeast Washington) with over 200 000 m^3 of high-level radioactive waste (HLW) in underground storage tanks. Several tanks are beyond or approaching their end of design life and some are suspected or confirmed to be leaking contaminants into the adjacent Columbia River.[1] The waste stabilization plan for permanent disposal is through borosilicate glass immobilization completed at the Hanford Waste Treatment and Immobilization Plant. A mixture containing glass formers and HLW is fed into joule-heated melters. Within the melters, the HLW mixture floats on top of molten glass forming a layer referred to as the "cold cap," where most reactions occur. The reaction-produced off-gases generate primary foam at the cold cap bottom, which limits heat transfer from the molten glass below, thus reducing the rate of melting and the overall process throughput. An understanding of primary foam kinetics and morphology as a function of feed time–temperature history is necessary to develop improved mathematical models of the cold cap.[2,3]

HLW glass feeds that contain varying compositions of glass formers and additives have been studied extensively in recent years through laboratory-scale investigations of their melting behavior.[4-11] One such feed, referred to as HWI-Al-19, was developed for the U.S. Department of Energy (DOE) Office of River Protection (ORP) by the Vitreous State Laboratory to vitrify high-aluminum HLW and has been shown to have desirable melting properties.[12] Hereafter, the term A19 will be used to denote a set of feeds based on HWI-Al-19 distinguished by slight alterations in the mass fractions of SiO_2, H_3BO_3, Li_2CO_3, and Na_2CO_3. These compositional variations lead to changes in the rheological properties of the final glass and the morphology of the cold caps that they produce.[10,13]

To study the feed to glass conversion, Hilliard and Hrma developed a method to estimate the porosity of the melting pellets by utilizing optical imaging and the density of the bulk and condensed phases.[14] Although this method was successfully used to study the kinetics of melting by analyzing the primary foam evolution and collapse,[3] it does not provide the morphology of primary foam bubbles during melting for use in the heat balance of the cold cap.

Instead, X-ray computed tomography (CT) imaging was recently used to examine the feed during heating,[15] providing its inner structure as a function of temperature. Morphological processing algorithms can be then applied to this data to extract quantitative information from the images, including the size and shape of bubbles and the void fraction of primary foam.[16,17] The method described herein supplements and improves currently used visual characterization of the melting feeds.

The motivation for this work relies upon the premise that, in the foaming stage, the bubbles in the pellet grow and coalesce in a similar manner as during the feed melting in a waste glass melter cold cap.[4] As the foam layer plays a key role in the transfer of heat from the melt pool, which ultimately impacts the melt rate of the feed, understanding this mechanism is paramount to increasing melter throughput. The purpose of this study is to provide an analysis of the foam morphology obtained from X-ray CT images of the feeds prepared.

2 | EXPERIMENT

2.1 | Feed preparation

Feed pellets were prepared using the method described by Lee et al.[13] Six modified A19 feeds were formulated with the constituents listed in Table 1 by combining all chemicals except quartz in deionized water, drying overnight at 105°C, and then milling the dried batches to powder. By changing the $SiO_2/(B_2O_3+Na_2O+Li_2O)$ ratio, where the chemical formulas signify the mass fractions of the oxide components in the glass, the feeds were formulated to make six glasses of estimated viscosities varying from 0.49 to 9.49 Pa s at 1150°C.[13,18] The mass fractions of all components (other than SiO_2, B_2O_3, Na_2O, and Li_2O) remained the same as in the A19-Original.[13] The mass fractions of B_2O_3, Na_2O, and Li_2O relative to each other were held constant (Table 2).

Quartz particles with diameters 63–75 μm were prepared from SIL-CO-SIL 250 by sieving, washing in water and ethanol, and drying at 90°C for 1 h. This quartz particle size range is found to avoid the problem of excessive foaming while dissolving acceptably quickly.[13] The quartz particles were then added to the feed powder to form the dry feed batch, from which 1.5-g cylindrical pellets of diameter 13 mm and height 6 mm were formed by pressing at 168 MPa for 90 s.

2.2 | X-ray CT imaging

The pellets were heated in a furnace at 10°C/min from 22°C to 1040°C. A tube voltage of 180 kV and a tube current of 90–160 μA were used, with 600 images captured per 360°C scan for all pellets except the A19-Original, where a tube current of 300 μA was used. Scans of the melting pellet were performed initially at 22°C and then every 20°C between 600°C and 1040°C. The images were provided as a time series of grayscale images, each through the central XZ plane of the pellet.

2.3 | Image segmentation and data extraction

For each melting pellet composition at each temperature, the X-ray CT measurements yielded a center-aligned grayscale cross-section characterized by random Gaussian noise and a roughly axially symmetric imaging artifact. This is shown in Figure 1A for the A19-Original pellet formulation at 820°C. Large ellipsoidal bubble cross sections are visible as dark regions, whereas the lighter-shaded condensed phase forms the approximately hemispherical profile of the pellet. The noise in the image produces apparent features on the order of 0.001 mm^2; this prevents the identification of bubbles or primary foam features at smaller scales.

Several image segmentation algorithms were explored in an attempt to process this raw data into a form amenable to quantitative analysis of the bubble morphology. Two complementary methods were ultimately applied and their results compared using Photoshop CS6: Method 1, grayscale thresholding and Method 2, manual segmentation. Method 1 began by cropping out the supporting structure and uniformly filling the central region to remove the imaging artifact from further analysis. Then, the maximum grayscale value of the background was used as the lower

TABLE 1 Formulations of feed pellets and estimated and measured glass viscosity[13,18] at 1150°C

Compositions (g)	A19-0	A19-1	A19-Original	A19-5	A19-7	A19-9
$Al(OH)_3$	371.79	371.79	371.79	371.79	371.79	371.79
H_3BO_3	**431.77**	**380.87**	**341.59**	**320.75**	**306.4**	**295.47**
Bi_2O_3	11.67	11.67	11.67	11.67	11.67	11.67
CaO	10.87	10.87	10.87	10.87	10.87	10.87
$Cr_4O_9H_6$	6.2	6.2	6.2	6.2	6.2	6.2
NaF	15	15	15	15	15	15
$Fe(OH)_3$	74.38	74.38	74.38	74.38	74.38	74.38
Li_2CO_3	**112.78**	**99.49**	**89.22**	**83.78**	**80.03**	**77.18**
NiO_2H_2	5.03	5.03	5.03	5.03	5.03	5.03
$FeH_6P_3O_6$	12.51	12.51	12.51	12.51	12.51	12.51
PbO	4.17	4.17	4.17	4.17	4.17	4.17
SiO_2	**151.45**	**190.96**	**221.45**	**237.62**	**248.76**	**257.24**
Na_2SO_4	3.6	3.6	3.6	3.6	3.6	3.6
ZrO_4H_4	5.53	5.53	5.53	5.53	5.53	5.53
$CaSiO_3$	97.07	97.07	97.07	97.07	97.07	97.07
NaOH	19.87	19.87	19.87	19.87	19.87	19.87
Na_2CO_3	**134.7**	**118.83**	**106.57**	**100.07**	**95.59**	**92.18**
$NaNO_2$	3.48	3.48	3.48	3.48	3.48	3.48
$NaNO_3$	12.4	12.4	12.4	12.4	12.4	12.4
$Na_2C_2O_4$	1.26	1.26	1.26	1.26	1.26	1.26
η(Pa s) at 1150° estimated[18]	0.49 (±0.15)	1.49 (±0.23)	3.49 (±0.49)	5.49 (±0.77)	7.49 (±1.09)	9.49 (±1.48)
η(Pa s) at 1150° measured[13]	N/A	1.79 (±0.30)	3.56 (±0.38)	5.36 (±0.01)	6.21 (±0.02)	9.00 (±0.03)
Sum (g)	1485.54	1444.97	1413.66	1397.06	1385.62	1376.91

Variations between feeds are highlighted in bold.

TABLE 2 The relative proportions of H_3BO_3, Li_2CO_3, and Na_2CO_3 were kept constant for all feeds

Compound	Mole fraction
H_3BO_3	0.714
Li_2CO_3	0.156
Na_2CO_3	0.130
Sum	1

bound of a threshold filter applied to the entire image. This "strong threshold" ensured that all remaining pixels almost certainly belong to the condensed phase of the melting pellet. This result is shown in Figure 1B. However, note that by comparing to the original image, it is clear that this procedure undersamples the condensed phase and dilates the bubble cross sections beyond their true sizes. Thus, while a light-shaded pixel likely lies within the condensed phase, it is less certain that a dark pixel lies within a bubble. This point will be revisited below.

In the second method, the bubbles were manually traced and filled, as shown in Figure 1C. During this procedure, only "obvious" bubbles (i.e., those that were clearly separated from other bubbles and had smooth edges) were traced and any bubbles that intersected the central artifact were excluded unless they were large enough to permit a reasonable extrapolation of their shape, assuming a circular boundary. The largest bubble in each image was invariably captured by this segmentation method. While this method relies on visual inspection and is therefore rather qualitative, the strict criteria for bubble identification allow this method to retain proper bubble cross-sectional areas following segmentation, as opposed to Method 1. Thus, these two methods supply different, although complementary, information. Method 1 provides a measure of porosity (as the ratio of dark pixels to total pixels within the pellet area) as well as a straightforward determination of pellet dimensions (width of base and pellet height). Method 2 provides maximum and average bubble sizes and areas. The latter

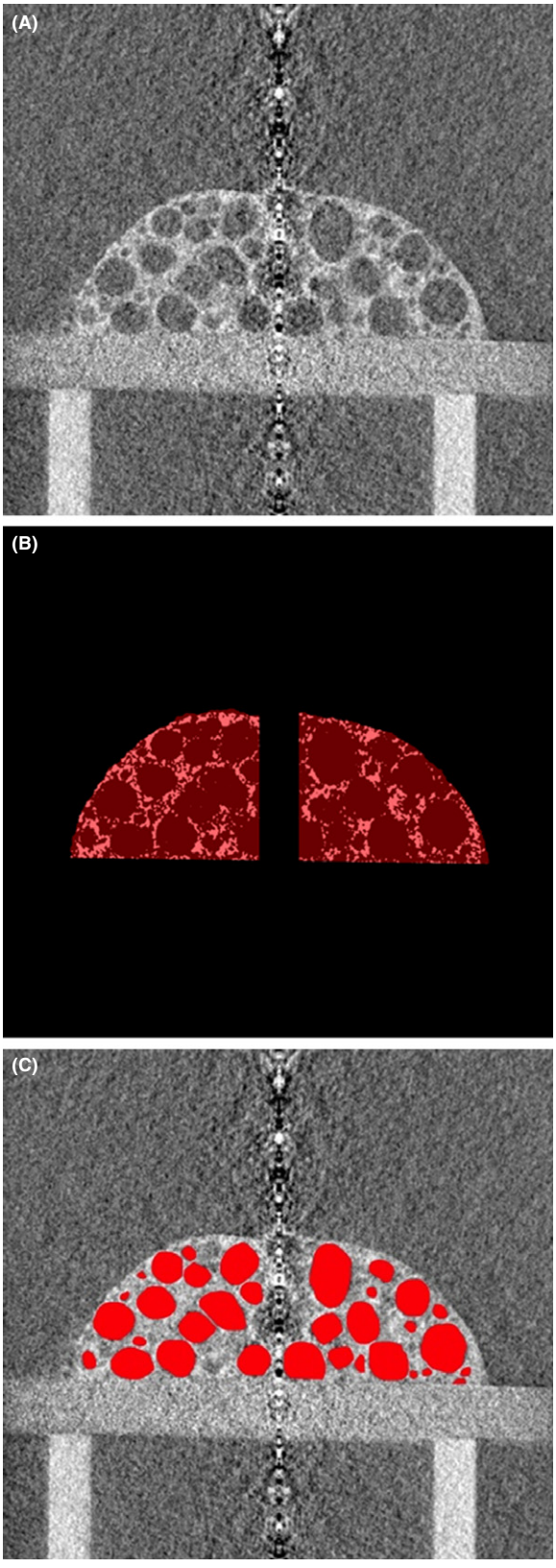

FIGURE 1 (A) Original X-ray CT image of the A19-Original feed pellet, (B) following grayscale threshold segmentation, and (C) following manual segmentation

values are necessarily overestimates because the X-ray CT images do not capture bubbles smaller than the features in the noise. Nevertheless, the as-calculated averages allow bubble size trends to be found and are therefore a useful semiquantitative measure of bubble morphology. A comparison of the methods is shown in Table 3. The bubble size estimates are potentially all underestimates, as the X-ray CT cross section does not necessarily intersect each bubble along its centerline.

From the grayscale threshold images, the following data were collected: total area of pellet profile A_T, and total void area A_V. The porosity, ϕ, or void fraction, is calculated as

$$\phi = A_V/A_T \quad (1)$$

2.4 | Evolved gas analysis

Thermal analysis was performed on an Agilent 6890N/5973N gas chromatograph with a mass spectrometric detector. Using a silica glass test tube, data were collected for a 1000-mg sample heated at a rate of 10°C/min under a helium dynamic atmosphere flowing at 50 mL/min.

3 | RESULTS AND DISCUSSION

3.1 | Visual comparison of pellet melting behavior

The complete collection of X-ray CT images is shown in Table 4, for all six pellet formulations at temperatures between 600°C and 1040°C. The raw images are shown with the manually traced bubbles superimposed.

A preliminary qualitative overview of the images shows that all pellets begin with the same shape (cylindrical, seen as a rectangular cross section through the center) with roughly the same dimensions, 6 mm high and 13 mm in diameter. Upon heating, the pellet profile areas initially stay almost constant, as the evolved gases freely escape through open porosity. A major component of the feed, H_3BO_3, starts to melt around 170°C. Pellets shrink as the temperature rises above 600°C, which is a result of attractive capillary forces arising from the presence of a liquid phase. The shrinkage stops as the liquid phase forming the primary melt closes the open porosity. At this point, evolved gases are trapped within the melt and major volume expansion of the pellet occurs due to bubble growth and expansion. This process is called primary foam evolution. As the temperature increases, the pellets become rounded with a hemispherical upper section and the base widens as the pellets melt. The pellet profile area approaches a maximum as the maximum bubble diameter approaches the height of the pellet. Thereafter, one or more of the largest bubbles burst through the upper surface,

TABLE 3 Comparison of segmentation methods for two pellet compositions at T=840°C. [Colour figure can be viewed at wileyonlinelibrary.com]

Method	A19-Original	A19-5
Manual	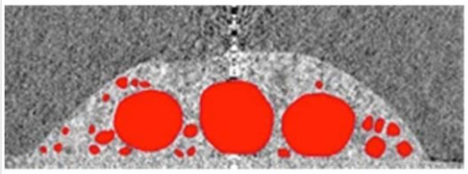	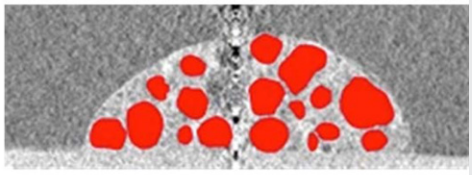
Strong threshold	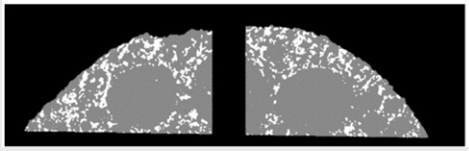	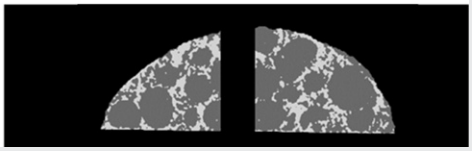

causing the pellet profile area to drop suddenly as the condensed phase collapses into the resulting void. Further gas evolution results in this pellet growth and collapse process repeating one or more times. By around 1000°C, the pellets have spread completely.

3.2 | Evolved gas analysis

To understand which gases contribute to the primary foam evolution, Figure 2 displays the evolved gas analysis performed at 10°C/min for the A19-Original feed (excluding water, which is released only below 450°C). Between 200°C and 700°C, a large amount of CO_2 and NO is evolving from the reactions of carbonates with boric oxide and dissolving silica, and the decomposition of $NaNO_3$, which is given by the following sequential reactions.[19]

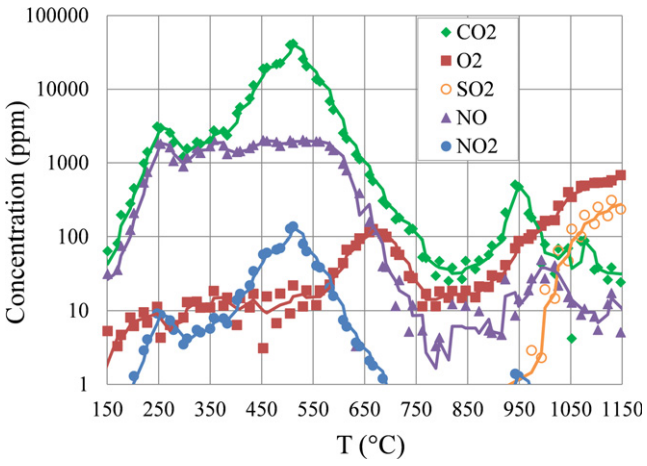

FIGURE 2 The evolved gas analysis of A19-Original.

$$NaNO_3 \rightarrow NaNO_2 + \frac{1}{2}O_2 \quad (2)$$

$$NaNO_2 \rightarrow \frac{1}{2}Na_2O + NO + \frac{1}{4}O_2 \quad (3)$$

The decomposition of sodium nitrate is accelerated by acidic oxides, such as silica.

The unexpected lack of significant oxygen evolution in the evolved gas analysis (EGA), together with NO, is likely caused by O_2 entering other reactions in the feed, such as with sodium oxalate or ferric hypophosphite, or by its physical dissolution in the melt with high basicity.

At approximately 760°C, the gas evolution from the feed "stops" as the open porosity closes and evolving gases are trapped in the foam (see images in Table 4). As the foam collapses above 880°C, a distinct CO_2 peak is observed, suggesting that CO_2 is the main contributor to the primary foam formation in the A19-Original feed.

Oxygen begins to evolve only above ~980°C, possibly from iron redox equilibrium and from the melt, which is oversaturated with O_2 from earlier batch reactions. There is no peak in O_2 evolution rate, which continues to climb until 1150°C. At around 1025°C, SO_2 generation also becomes appreciable. The relative contributions of the remaining gases are negligible compared to those of CO_2, O_2, and SO_2.

3.3 | Primary foam evolution and collapse

Figure 3 shows the pellet profile area as a function of temperature for all six formulations, normalized to the height of the pellet at 600°C so that only relative changes in height are considered. Throughout this report, normalized lengths and areas are calculated by dividing by the length or area at 600°C for the given pellet formulation. The

temperatures corresponding to the initial minimum in the pellet profile area and the following maximum are referred to as the primary foam temperature, T_P, and the collapse temperature, T_C.[20] This terminology is used here to be consistent with previous investigations of feed pellet melting behavior. Let us mention that the ~60°C temperature differences in the foam onset (~760°C in Figure 2, ~700°C in Figure 3) and collapse (~880°C in Figure 2, ~820°C in Figure 3) are caused by the different thermocouple positions and calibration procedures used in the two separate experiments.

The profile area curves in Figure 3, which are in good agreement with those observed in previous pellet expansion studies,[4,13] reveal that as the amount of SiO_2 (and thus final melt viscosity) increases, T_P, T_C, and the corresponding normalized pellet area $A_T(T_C)$ also increase. Moreover, whereas T_P increases, the corresponding $A_T(T_P)$ values are roughly equal. The trends shown in Figure 4 result from a later formation of primary borosilicate melt[13] and a higher melt viscosity, which is caused by the decreasing amounts of molten salts (Li_2CO_3, Na_2CO_3, and H_3BO_3) in the feeds with higher SiO_2 content.

TABLE 4 X-ray CT images with manually traced bubbles superimposed.

T (°C)	A19-0	A19-1	A19-Original	A19-5	A19-7	A19-9
600						
620						
640						
660						
680						
700						
720						
740						
760						
780						
800						

Continues

TABLE 4 Continued

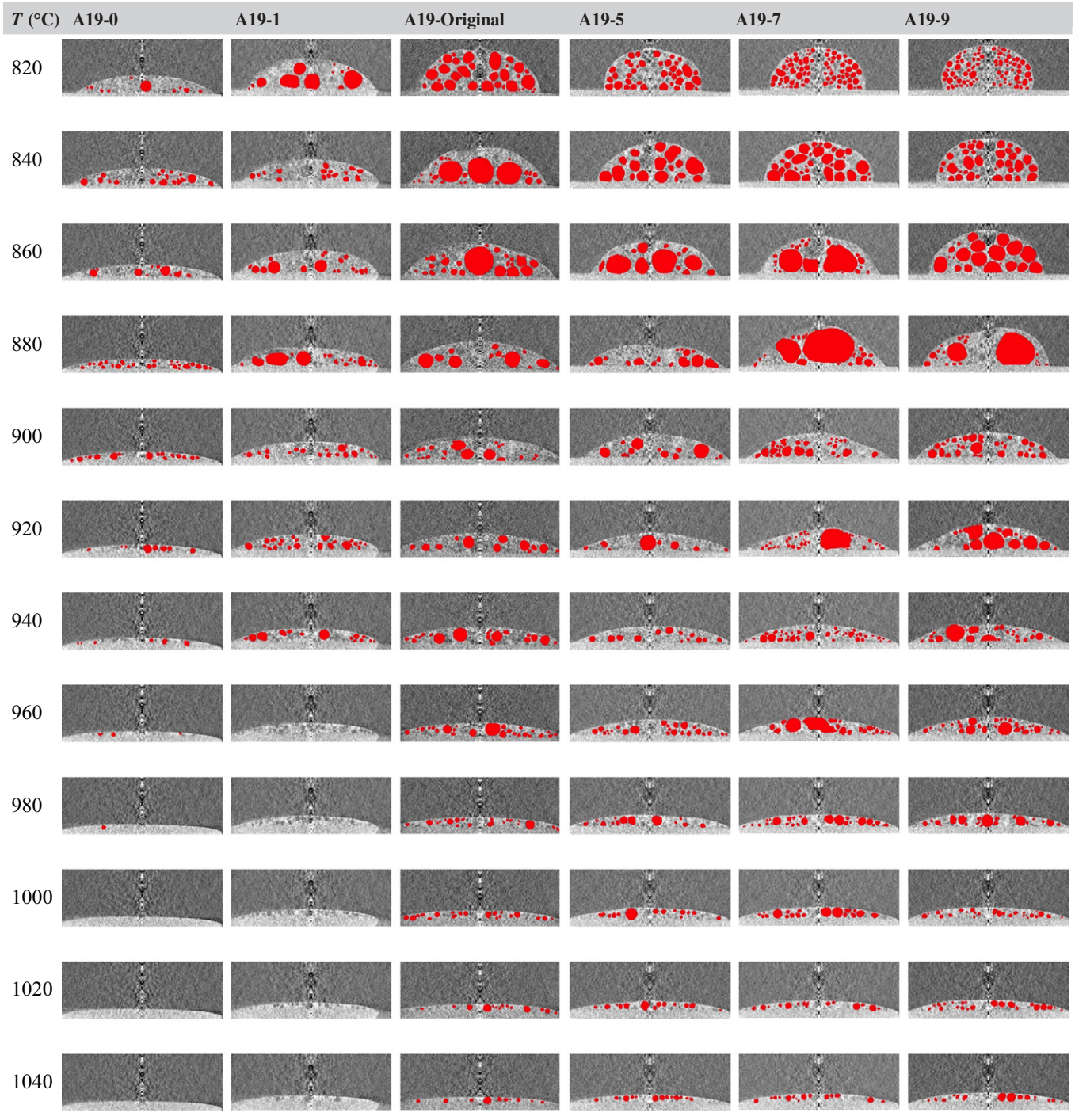

To understand the increase in T_C and the pellet volume at T_C with increasing viscosity, it is necessary to weigh several competing factors. First, the A19 feed viscosity is controlled through variations in the SiO_2 mass fraction of the pellets, which is accompanied by variations in the SiO_2 mass fraction w_{SiO2} in the final waste glass. As w_{SiO2} and viscosity increase in the samples (see Figure 5), the Li_2CO_3, H_3BO_3, and Na_2CO_3 contents decrease. Therefore, less CO_2 can be evolved from the decomposition of Li_2CO_3 or the calcination of Na_2CO_3 and less water can be liberated from H_3BO_3. Thus, as viscosity increases, the total volume of off-gases produced over the entire course of melting decreases. However, this does not mean the gas evolution rate will necessarily decrease in the observed foaming region. This could be related to the fact that the primary melt is formed at higher temperatures, thus affecting the kinetics of decomposition reactions and shifting the gas evolution to higher temperatures.

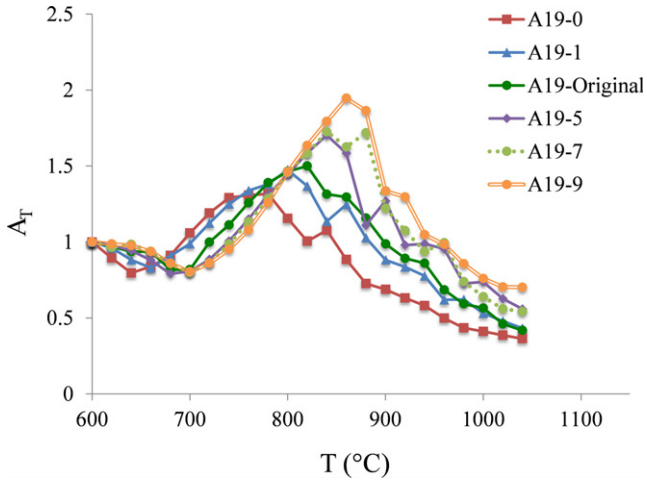

FIGURE 3 Pellet profile area as a function of temperature for six pellet formulations.

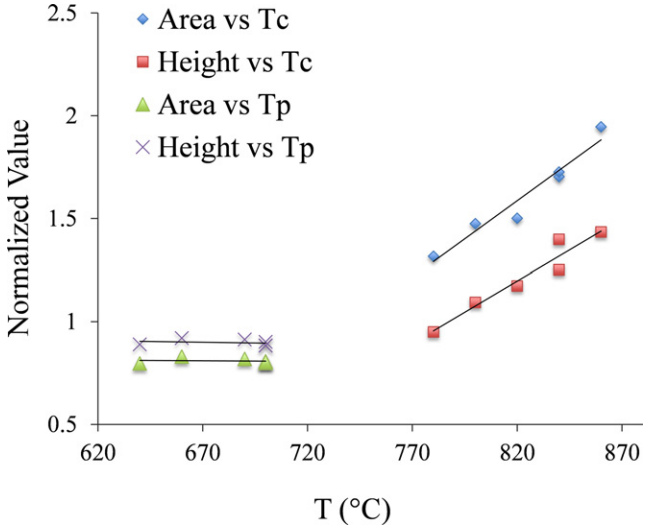

FIGURE 4 Pellet area and pellet height (normalized to values at 600°C) as a function of primary foam temperature (left) and initial collapse temperature (right).

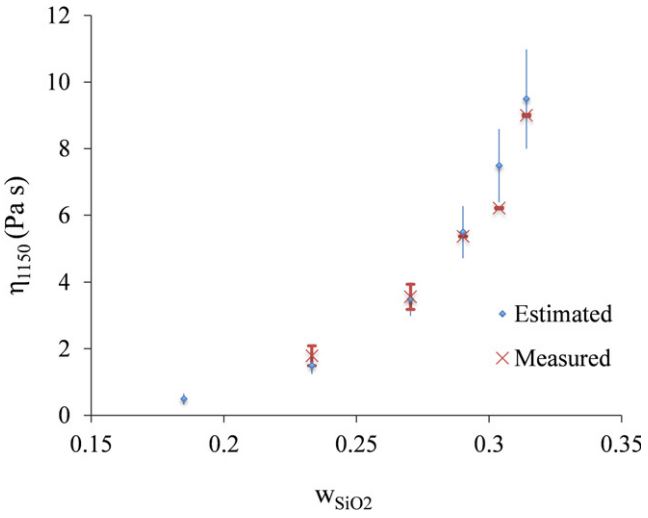

FIGURE 5 Model-estimated and measured viscosities at 1150°C as a function of SiO_2 mass fraction in the final waste glass.

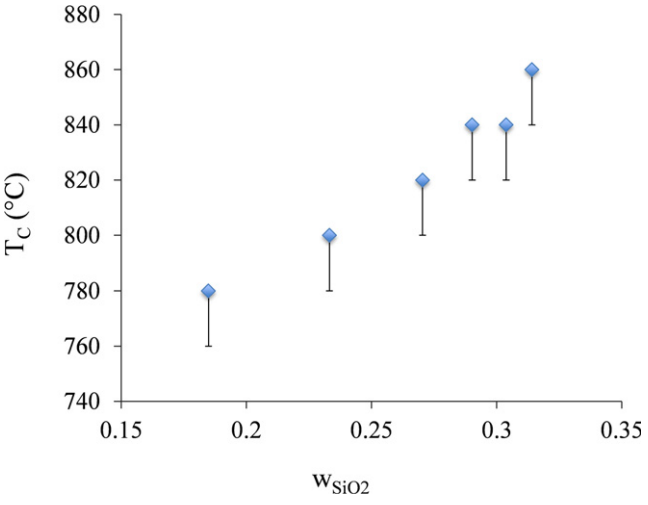

FIGURE 6 Initial collapse temperature as a function of final waste glass composition.

The increase in T_C and pellet area with higher SiO_2 content can be interpreted as a result of increased melt viscosity, which stabilizes the foam. Because viscosity decreases with temperature, pellets richer in SiO_2 must be heated to a higher temperature before the viscosity is lowered to the point that the pellets start to collapse via drainage of the melt from the bubble walls. This is illustrated in Figure 6, which shows that the collapse temperature increases with w_{SiO2} (see also Figure 3). The lower error bars have a magnitude of 20°C and are included to account for the fact that, for each pellet, the initial collapse may have occurred in the interval between X-ray CT images.

Another explanation for the pellet area increase for higher viscosity feeds is motivated by the EGA results presented in Figure 2 showing that O_2 production becomes appreciable for the A19-Original feed above 950°C. It is possible that as the collapse temperature T_C shifts to higher temperatures for high viscosity feeds, O_2 can be captured in the foam along with CO_2.

3.4 | Calculated porosity and bubble size

As described in chapter 2C, the void fraction, ϕ, is defined as the ratio of dark pixels to total pixels within the pellet profile. Figure 7 displays the porosity of pellets as a function of temperature. The porosity initially increases sharply with temperature, followed by a more gradual decline as the foam

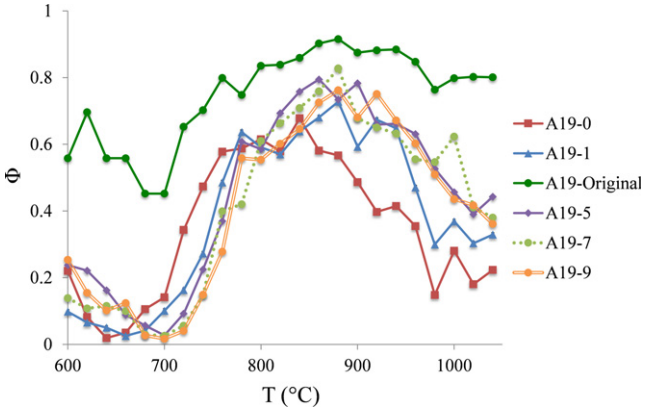

FIGURE 7 Two-dimensional porosity as a function of temperature.

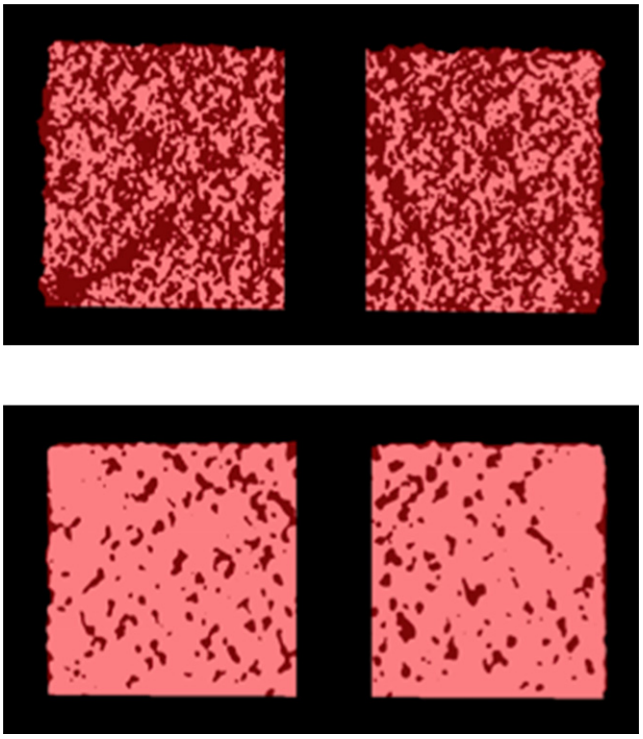

FIGURE 8 Comparison of the threshold segmentation result for the A19-Original pellet (top, 300 μA tube current) and the A19-7 pellet (bottom, 90–160 μA). Both scans are at 600°C.

collapses and bubbles are released. The results are in a good agreement with values obtained utilizing optical imaging and the density of the bulk and condensed phases.[21] Regarding the anomalous result calculated for A19-Original: unlike all other pellets, the A19-Original pellet was scanned with a 300-μA tube current, resulting in a higher-resolution grayscale image being used for data analysis. The higher contrast between the light and dark pixels skewed the results of the threshold applied during segmentation and, as a consequence, systematically increased the calculated porosity by

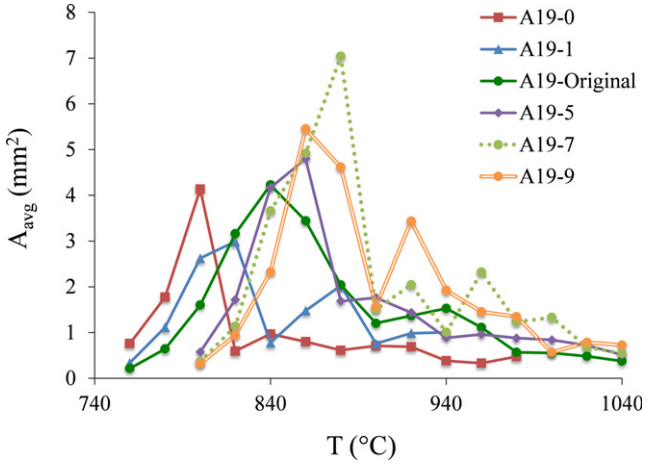

FIGURE 9 Average area of the largest 10 bubbles as a function of temperature.

undersampling the condensed phase. This is shown in the side-by-side comparison in Figure 8. Therefore, we discard the results of threshold segmentation for the A19-Original pellet in subsequent analysis.

Figure 9 displays the average area of the largest 10 bubbles, A_{avg}. This value, rather than the average area of all bubbles, was calculated to avoid the error introduced by the identification of small bubbles during manual segmentation. Figure 10 shows the diameter of the largest bubble, D_{max}, along with the pellet height.

Figure 9 shows that the A_{avg} value peaks several times during heating, with each successive maximum generally being smaller than the previous. The same trend is observed in Figure 10 for the maximum bubble diameter. This gradual reduction in average and maximum bubble areas is caused by bubbles bursting through the surface of the pellet and the fact that the height of a bubble cannot exceed the height of the pellet.

The fact that bubbles cannot exceed the size of the pellet without causing collapse also slightly limits the nature of data that can be extracted from this study. In particular, when the sizes of the largest bubbles approach the pellet height, the observed bubble sizes no longer correspond to those observed in an actual melter. At the cold cap bottom in the melter, bubbles are free to expand further and form larger gas cavities, which are swept away by convective forces exerted by the molten glass flow, escaping at the cold cap edge or through the vent holes. Thus, pellet studies should not be used to characterize the foam morphology at temperatures above the initial collapse temperature. An X-ray image of a continuous laboratory-scale melter with a real cold cap could provide more details.

The measured temperature-dependent width of the pellet base can estimate how readily the various A19 feed

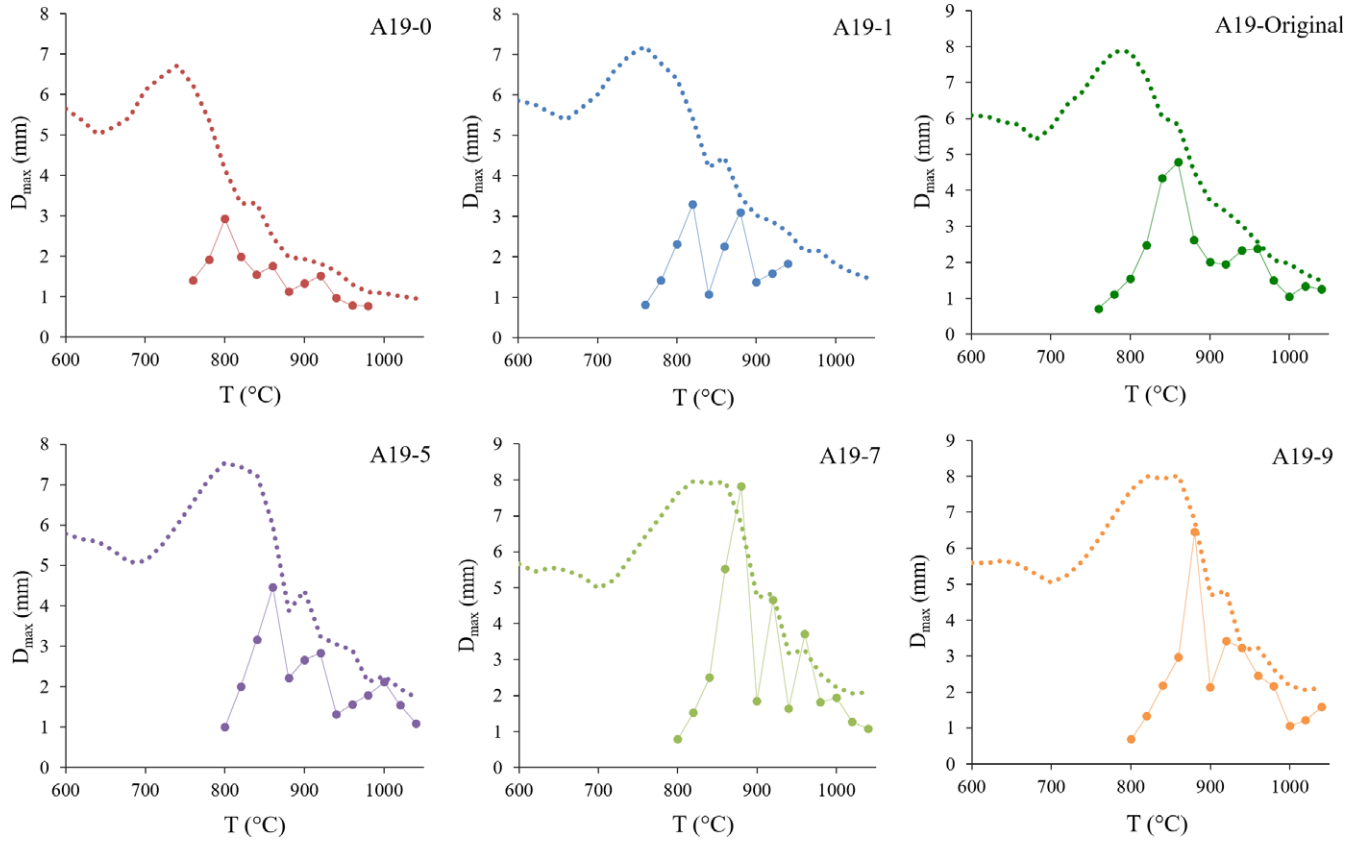

FIGURE 10 The solid curves show the maximum bubble diameter as a function of temperature, whereas the dotted lines show the corresponding pellet height.

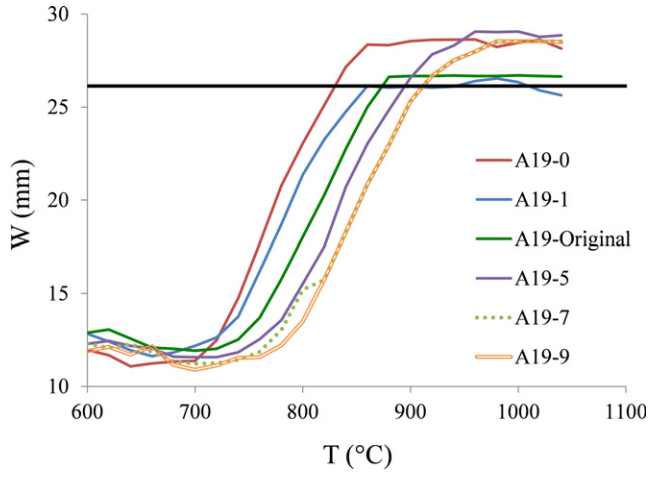

FIGURE 11 Width of pellet base as a function of temperature.

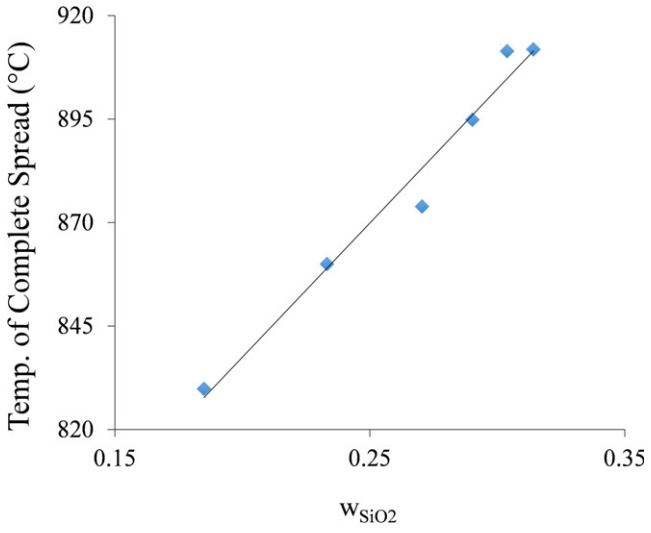

FIGURE 12 Temperature of complete spread as a function of SiO_2 content in the final waste glass.

compositions melt. This is shown in Figure 11. For all formulations, after a brief decrease, the width of the pellet base increases to span the entire imaged region. This occurs between approximately 700°C and 900°C. The dark horizontal line in Figure 11 marks a cutoff where the pellet base reaches 26 mm in width. The linearly interpolated temperature where each feed reaches this threshold is plotted in Figure 12 as a function of w_{SiO2}. With increasing SiO_2 content, the attainment of total spread was observed at higher temperature.

4 | CONCLUSIONS AND FUTURE WORK

The morphologies of melting pellets of a simulated high-aluminum HLW feed for a glass melter obtained using X-ray CT imaging were studied as functions of temperature and SiO_2 mass fraction in the final waste glass. The pellets, initially cylindrical in shape and heated at 10°C/min, were imaged at 20°C intervals from 600°C to 1040°C. To track morphology during the melting process, cross sections obtained through the central profile of the pellet and parallel to its axis were digitally segmented into gas and a condensed phase. The primary foam morphology was characterized by calculating pellet profile area, average and maximum bubble areas, maximum bubble diameter, and void fraction. Two complementary methods were applied and their results compared: (i) grayscale thresholding and (ii) manual segmentation.

The pellets initially underwent a decrease in volume (reaching a minimum at the primary foam temperature, T_P) above which the entrapment of evolved batch gases led to primary foam evolution and pellet expansion. The pellets then collapsed at T_C and expanded again several times. The experimental data suggest that increasing the SiO_2 mass fraction in the final waste glass shifts both the onset of primary foam evolution and the foam collapse to higher temperatures by delaying the connection of the borosilicate melt and forming primary melt with higher viscosity. Normalized pellet area and pellet height at T_P were independent of T_P, whereas their values at T_C increased linearly with T_C. In addition, higher viscosity pellets take more time and a higher temperature to fully spread, suggesting that lower viscosity feeds will melt more rapidly.

The evolved gas analysis revealed that CO_2 is the main component of the primary foam gas, with possible contributions from O_2 for feeds with higher viscosity. The maximum bubble size in the foam increased due to continuous gas evolution, thermal expansion, and internal coalescence of foam bubbles. The maximum bubble size was inherently limited by the size of the pellets used in the experiment. Larger-scale studies, such as X-ray CT imaging of a continuous laboratory-scale melter with an in situ-formed cold cap, are needed to gain a more accurate understanding of foam morphology above T_C, for which the results of this study no longer apply.

Plans for future analysis include comparison of the two-dimensional pellet profiles with three-dimensional volume data from X-ray CT measurements. The results presented in this work will be used to update the mathematical cold cap model by employing the evaluated foam morphology in the heat balance of the cold cap and improving the understanding of primary foam formation and collapse.

ACKNOWLEDGMENTS

This work was supported by Albert Kruger from DOE ORP's Waste Treatment and Immobilization Plant Project and by the DOE Office of Science, Office of Workforce Development for Teachers and Scientists under the Science Undergraduate Laboratory Internship program. The authors are grateful to DOE's Office of Environmental Management (EM) International Program for funding of the proposal submitted from the ORP, as a part of the portfolio managed by Rodrigo Rimando of EM. The X-ray tomography was performed by Takuma Naito, Yukihiro Yoshida, and Tetsuo Kishi. The work at Idaho National Laboratory was performed by Battelle Energy Alliance, LLC under the DOE Idaho Operations Contract DE-AC07-05ID14517. Many thanks to Edmund Han of Rutgers University for providing insightful discussions of glass melting processes and to Kai Xu of Wuhan University of Technology for working with Tetsuji Yano on the X-ray CT imaging.

REFERENCES

1. Kirkbride RA. Tank Waste Remediation System Operation and Utilization Plan. In: Vol. I. HNF-SD-WM-SP-012. Richland, Washington: Numatec Hanford Corporation; 1999:1-1-1-5. https://www.osti.gov/scitech/biblio/16944.
2. Guillen DP, Beers CJ. Modeling the vitrification of hanford tank waste. *Trans Am Nucl Soc*. 2015;112.
3. Pokorny R, Hilliard ZJ, Dixon DR, et al. One dimensional cold cap model for melters with bubblers. *J Am Ceram Soc*. 2015;98:3112-3118.
4. Hrma P, Schweiger MJ, Humrickhouse CJ, et al. Effect of glass-batch makeup on the melting process. *Ceram-Silik*. 2010;54:193-211.
5. Pokorny R, Hrma P. Mathematical modeling of cold cap. *J Nucl Mater*. 2012;429:245-256.
6. Chun J, Pierce DA, Pokorny R, Hrma P. Cold-cap reactions in vitrification of nuclear waste glass: experiments and modeling. *Thermochim Acta*. 2013;559:32-39.
7. Rodriguez CP, Chun J, Schweiger MJ, Kruger AA, Hrma P. Application of evolved gas analysis to cold-cap reactions of melter feeds for nuclear waste vitrification. *Thermochim Acta*. 2014;592:86-92.
8. Hrma P. Conversion of nuclear waste into nuclear waste glass: experimental investigation and mathematical modeling. *Procedia Mater Sci*. 2014;7:117-123.
9. Johnson FC, Choi AS, Miller DH, Immel DM. *Comparison of HLW Glass Melting Rate Between Frit and Glass Forming Chemicals Using X-Ray Computed Tomography*. SRNL-STI-2014-00562 Rev. 0. Aiken, SC: U.S. Department of Energy; 2015.
10. Marcial J, Chun J, Hrma P, Schweiger M. Effect of bubbles and silica dissolution on melter feed rheology during conversion to glass. *Environ Sci Tech*. 2014;48:12173-12180.
11. Matlack KS, Gan H, Chaudhuri M, et al. *DM100 and DM1200 Melter Testing with High Waste Loading Glass Formulations for Hanford High-Aluminum HLW Streams*. VSL-10R1690-1, Rev. 0.

Washington, DC: Vitreous State Laboratory, The Catholic University of America; 2010.
12. Kruger AA, Joseph I, Pegg IL, Matlack KS, Callow RA, Kot WK. *Final Report – Testing of Optimized bubbler Configuration for HLW Melter VSL-13R2950-1*, Rev. 0, ORP-56287. Richland, WA:Hanford Site; 2013.
13. Lee S, Hilliard Z, Heilman-Moor JS, et al. *The Effect of Quartz Size and Melt Viscosity on HLW Melter Feed Using Pellet Test Response*, WM2016 Conference. Phoenix, Arizona; 2016.
14. Hilliard Z, Hrma P. A method for determining bulk density, material density and porosity of melter feed during nuclear waste vitrification. *J Am Ceram Soc*. 2016;99:98-105.
15. Watanabe K, Yano T, Takeshita K, Minami K, Ochi E. X-ray CT imaging of vitrified glasses containing simulant radioactive wastes: Structure and chemical reactions of glass beads and wastes in the cold cap. *Glass Technol: Eur J Glass Sci Technol A*. 2012;53:273-278.
16. Jean S. Introduction to mathematical morphology. *Compute Vision Graphics Image Process*. 1986;35.3:283-305.
17. Jean S., Soille P, eds. Mathematical morphology and its applications to image processing. *Springer Sci & Business Media*. 2012;2:25-36
18. Hrma PR, Han SS. Effect of glass composition on activation energy of viscosity in glass-melting-temperature range. *J Non Cryst Solids*. 2012;358:1818-1829.
19. Hoshino Y, Utsunomiya T, Abe O. The thermal decomposition of sodium nitrate and the effects of several oxides on the decomposition. *Bull Chem Soc Jpn*. 1981;54:1385-1391.
20. Pokorny R, Hrma P. Model for the conversion of nuclear waste melter feed to glass. *J Nucl Mater*. 2014;445:190-199.
21. Lee S, VanderVeer BJ, Hrma P, et al. Effects of heating rate, quartz particle size, viscosity, and form of glass additives on high-level waste melter feed volume expansion. *J Am Ceram Soc*. 2016. doi:10.1111/jace.14629.

How to cite this article: Harris WH, Guillen DP, Klouzek J, et al. X-ray tomography of feed-to-glass transition of simulated borosilicate waste glasses. *J Am Ceram Soc*. 2017;00:1–12. https://doi.org/10.1111/jace.14895